Guiding-Based Importance Sampling for Walk on Stars

TIANYU HUANG, Tsinghua University, China JINGWANG LING, Tsinghua University, China SHUANG ZHAO, University of California, Irvine, USA FENG XU*, Tsinghua University, China

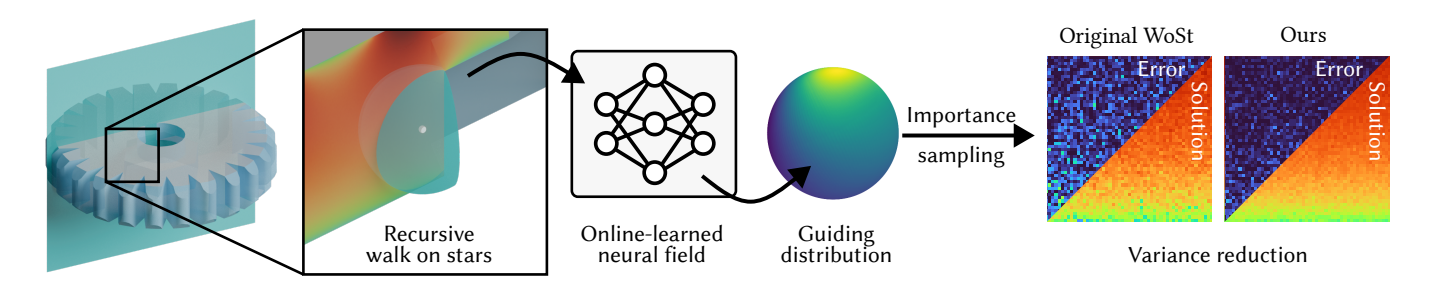


Fig. 1. An overview of our core method: We utilize an online-learned neural field to model the space-conditioned importance sampling distribution (guiding distribution) for the recursive term of the walk on stars (WoSt) estimator, achieving effective variance reduction.

Walk on stars (WoSt) has shown its power in being applied to Monte Carlo methods for solving partial differential equations, but the sampling techniques in WoSt are not satisfactory, leading to high variance. We propose a guiding-based importance sampling method to reduce the variance of WoSt. Drawing inspiration from path guiding in rendering, we approximate the directional distribution of the recursive term of WoSt using online-learned parametric mixture distributions, decoded by a lightweight neural field. This adaptive approach enables importance sampling the recursive term, which lacks shape information before computation. We introduce a reflection technique to represent guiding distributions at Neumann boundaries and incorporate multiple importance sampling with learnable selection probabilities to further reduce variance. We also present a practical GPU implementation of our method. Experiments show that our method effectively reduces variance compared to the original WoSt, given the same time or the same sample budget. Code and data will be released.

CCS Concepts: • Mathematics of computing \to Partial differential equations; Probabilistic algorithms; • Computing methodologies \to Rendering.

Additional Key Words and Phrases: Importance sampling, walk on stars, Monte Carlo methods

1 Introduction

Partial differential equations (PDEs) are commonly used to model various phenomena such as heat transfer, wave propagation, and fluid dynamics in physics, engineering, and computer graphics. Recently, Monte Carlo methods for solving PDEs have been gaining attention due to their advantages, such as eliminating the need for meshing, handling intricate geometric structures, and supporting local evaluations. This series of methods began with Sawhney and Crane [2020], who applied walk on spheres (WoS) [Muller 1956] to

Authors' Contact Information: Tianyu Huang, Tsinghua University, Beijing, China, huang-ty21@mails.tsinghua.edu.cn; Jingwang Ling, Tsinghua University, Beijing, China, lingjw20@mails.tsinghua.edu.cn; Shuang Zhao, University of California, Irvine, IVSA, shz@ics.uci.edu; Feng Xu, Tsinghua University, Beijing, China, xufeng2003@gmail.com.

the Dirichlet Poisson problem, which was later extended by *walk on stars (WoSt)* [Miller et al. 2024b; Sawhney et al. 2023] to support Neumann boundary conditions. These advancements have been applied to a wide range of applications, including volume rendering [Qi et al. 2022], fluid simulation [Jain et al. 2024; Rioux-Lavoie et al. 2022], thermal simulation [De Lambilly et al. 2023], robotics [Muchacho and Pokorny 2024], machine learning [Nam et al. 2024], shape modeling [de Goes and Desbrun 2024], and infrared rendering [Bati et al. 2023].

However, WoSt suffers from high variance and slow convergence, especially for problems with complex domains or boundary conditions. To address this problem, several recent methods [Bakbouk and Peers 2023; Li et al. 2023; Miller et al. 2023; Qi et al. 2022] have adopted variance reduction techniques originated in Monte Carlo rendering [Müller et al. 2021; Veach and Guibas 1995a] for WoSt. The importance sampling family is effective for variance reduction in rendering, and so far, there have been explorations to importance sample the non-recursive Neumann and source contributions [Sawhney and Crane 2020; Sawhney et al. 2023] of WoSt. However, the recursive term of WoSt, lacking a closed form or shape information before computation, poses a challenge for traditional importance sampling techniques such as Next Event Estimation (NEE) [Immel et al. 1986; Kajiya 1986]. As it currently stands, the recursive term can only be sampled using uniform directional sampling.

We believe adaptive importance sampling techniques can handle the recursive term, as their online learning approach enables operation without prior knowledge of the distribution shape or modifications to the formulation. Here, a representative approach in rendering is path guiding [Herholz et al. 2019; Müller et al. 2017; Vorba et al. 2014] which uses the observations from earlier samples to optimize the importance sampling distribution (guiding distribution), and uses the distribution to generate subsequent samples. Furthermore, recent advances using neural fields to encode space-conditioned parametric guiding distributions [Dong et al. 2023; Huang et al.

^{*}Corresponding author.

2024] have demonstrated exceptional performance in variance reduction, indicating the potential to apply path guiding to WoSt for better reducing variance.

In this paper, we introduce a guiding-based importance sampling method to reduce the variance of WoSt. Specifically, we approximate the directional distribution of the recursive term of WoSt using von Mises-Fisher (vMF) mixtures. The mixtures are decoded by a lightweight neural field that takes space coordinates as input. Then we employ gradient-based online learning on the neural field to optimize vMF mixtures. This approach effectively handles high-frequency variations in the solution field. Besides, the walk behavior is special at Neumann boundaries in WoSt, so we propose a sample reflection technique on vMF mixtures to represent guiding distributions at Neumann boundaries. This technique effectively reduces variance around Neumann boundaries compared to trivial approaches. Additionally, we explore multiple importance sampling (MIS) with learnable selection probabilities in WoSt, which guarantees unbiasedness and adaptively adjusts the balance between guiding and uniform directional sampling, further reducing variance. We present a practical GPU implementation of our method, enabling efficient parallelization including neural field training and geometric queries.

Our contributions are

- a guiding-based importance sampling method for the WoSt estimator.
- a sample reflection technique for guiding distributions at Neumann boundaries, and
- learnable selection probabilities for MIS that adaptively balance guiding and uniform directional sampling in WoSt.

We compare our method with the original WoSt using several 2D and 3D problems under equal time or equal sample settings, demonstrating that our approach effectively reduces variance.

2 Related Work

2.1 Monte Carlo Methods for Solving PDEs

Recent exploration of Monte Carlo methods for solving partial differential equations (PDEs) has gained significant attention in the graphics community, as they offer advantages over traditional methods like finite element (FEM) and finite difference (FDM) by circumventing spatial discretization challenges while providing better flexibility and performance. The pioneering work, Monte Carlo Geometry Processing [Sawhney and Crane 2020] revisits Walk on Spheres (WoS) [Muller 1956] to solve linear elliptic equations with Dirichlet boundary conditions, which is later extended to walk on stars (WoSt) [Ermakov and Sipin 2009; Sawhney et al. 2023; Simonov 2008] to handle Neumann and Robin [Miller et al. 2024b] boundary conditions. Under the WoS and WoSt frameworks, the methods are further generalized to address problems with spatially varying coefficients [Sawhney et al. 2022], surface PDEs [Sugimoto et al. 2024b], and infinite domains [Nabizadeh et al. 2021]. Monte Carlo methods have demonstrated broad applicability in both forward [Bati et al. 2023; de Goes and Desbrun 2024; De Lambilly et al. 2023; Jain et al. 2024; Muchacho and Pokorny 2024; Nam et al. 2024; Rioux-Lavoie et al. 2022] and inverse [Miller et al. 2024a; Yilmazer et al. 2024; Yu et al. 2024] PDE problems. In parallel with WoS and WoSt, Walk on

Boundary [Sugimoto et al. 2023], another Monte Carlo estimator for PDEs, has been revisited and applied to fluid simulations [Sugimoto et al. 2024a]. Similar to Monte Carlo rendering, Monte Carlo PDE solvers face the challenges of slow convergence and high variance. Various methods, including neural caches [Li et al. 2023], bidirectional formulation [Qi et al. 2022], mean value caching [Bakbouk and Peers 2023], and boundary value caching [Miller et al. 2023], have been proposed to address these issues. So far, no existing method has performed importance sampling on the recursive term of the WoSt estimator. Our guiding-based method explores using online-learned distributions to perform importance sampling on the recursive term to reduce variance.

2.2 Path Guiding in Rendering

In Monte Carlo rendering, path guiding is a data-driven adaptive sampling scheme which learns the importance sampling distribution (guiding distribution) from previous samples to improve subsequent samples, thus reducing variance. Here, the guiding distribution is conditioned on space and normalized across directions. Research in path guiding primarily focuses on how to represent, store, and optimize the guiding distribution across spatial, and recently, temporal domain [Dong et al. 2024]. Early attempts in this field include constructing spatially cached histograms [Jensen 1995], cones [Hey and Purgathofer 2002] or Gaussian mixtures [Vorba et al. 2014]. A wellknown recent work is [Müller et al. 2017], which utilizes SD-trees to implement path guiding practical for production environments. Subsequent works have considered volume rendering [Herholz et al. 2019], caustics [Fan et al. 2023; Li et al. 2022], path space [Reibold et al. 2018], variance-aware sampling [Rath et al. 2020], and physicsbased differentiable rendering [Fan et al. 2024]. In the deep learning era, path guiding based on neural networks have also been explored, such as employing convolutional neural networks to reconstruct radiance fields [Huo et al. 2020; Zhu et al. 2021] or using invertible neural networks to model complex distributions [Müller et al. 2019]. Recently, methods utilizing neural fields to encode parameterized guiding distributions [Dong et al. 2023; Huang et al. 2024] have emerged as the state-of-the-art in the field of path guiding. These methods ensure high performance while avoiding the parallax issues inherent in traditional discrete spatial storage structures. Since path guiding does not require a prior distribution, it is particularly well-suited to our problem. Our work is inspired by path-guiding techniques in rendering, with unique improvements tailored for 2D and 3D PDE problems, including reflection transformations on the guiding distribution to handle Neumann boundaries and multiple importance sampling with learnable selection probabilities to combine the uniform directional sampling.

3 Background

3.1 Linear Elliptic Equations

Walk on stars (WoSt) primarily targets linear elliptic equations, which encompass a wide variety of forms. However, the structure of WoSt remains largely consistent across different formulations. We thus focus on the most typical case—the Poisson equation with

Dirichlet and Neumann boundary conditions:

$$\begin{split} \Delta u(x) &= f(x) &\quad \text{on } \Omega, \\ u(x) &= g(x) &\quad \text{on } \partial \Omega_{\mathrm{D}}, \\ \frac{\partial u(x)}{\partial n_{\mathrm{X}}} &= h(x) &\quad \text{on } \partial \Omega_{\mathrm{N}}, \end{split} \tag{1}$$

where the boundary of the domain $\Omega \subset \mathbb{R}^d$ (d = 2,3) is partitioned into a Dirichlet part $\partial\Omega_D$ and a Neumann part $\partial\Omega_N$ with prescribed values g and h (resp.). Δ is the negative-semidefinite Laplacian, $u: \Omega \to \mathbb{R}$ is the unknown solution, and $f: \Omega \to \mathbb{R}$ is a source term. This equation can describe, e.g., the steady-state temperature distribution, where f represents the heat source or sink, *q* corresponds to the temperature on the boundary, and *h* denotes the heat flux on the boundary.

The Walk on Stars (WoSt) Estimator

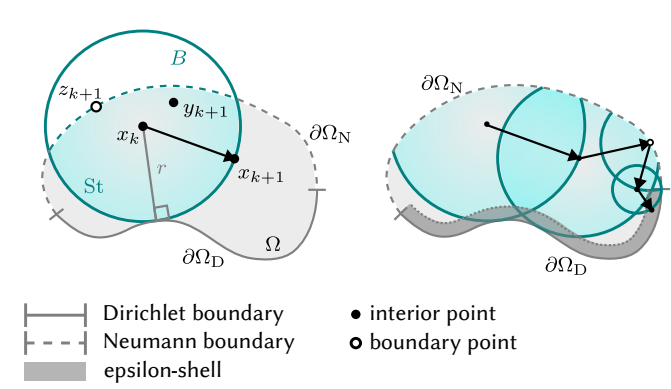


Fig. 2. Illustration of the WoSt estimator in 2D. Left: An illustration of a $\mathit{step.}\ x_k$ is the query point, x_{k+1} is the next walk location, y_{k+1} is the source sample point, and z_{k+1} is the Neumann boundary sample point. Right: An entire walk of WoSt, which iteratively samples the next walk location until it reaches the Dirichlet boundaries' ϵ -shell.

We define the ϵ -shell $\partial\Omega_{\mathrm{D}}^{\epsilon}:=\{x\in\Omega:\min_{y\in\partial\Omega_{\mathrm{D}}}\|x-y\|\leq\epsilon\}$ for a manually specified small $\epsilon>0$, which is the region where the walks terminate. The solution $u(x_k)$ at any query point $x_k \in \Omega \setminus \partial \Omega_D^{\epsilon}$ for Eq. 1 can be obtained using the following single-sample WoSt estimator [Sawhney et al. 2023]:

$$\langle u(x_k) \rangle = \frac{P^B(x_k, x_{k+1}) \langle u(x_{k+1}) \rangle}{\alpha(x_k) p^{\partial St(x_k, r)}(x_{k+1})} - \langle N \rangle + \langle S \rangle,$$

$$\langle N \rangle = \frac{G^B(x_k, z_{k+1}) h(z_{k+1})}{\alpha(x_k) p^{\partial StN(x_k, r)}(z_{k+1})},$$

$$\langle S \rangle = \frac{G^B(x_k, y_{k+1}) f(y_{k+1})}{\alpha(x_k) p^{St(x_k, r)}(y_{k+1})},$$
(2)

where $\langle N \rangle$ and $\langle S \rangle$ are non-recursive Neumann and source contributions, resp.; B is a ball centered at x_k with radius r; the radius r equals to the smaller value between the distance from x_k to $\partial\Omega_{\rm D}$ and the distance from x_k to the nearest silhouette on $\partial \Omega_N$; the star-shaped region St := $B \cap \Omega$, and ∂ StN denotes the Neumann boundaries of St; $\alpha(x_k)$ is set to 1 if x_k lies within St, 1/2 if it lies on the boundary of St, and 0 if it lies outside St; G^B denotes the Green's function

defined over the sphere B [Sawhney et al. 2023, Eq. 24], while P^B , the Poisson kernel on B, is defined as $P^B = \partial G^B / \partial n$; p represents the PDF of the sampler. The illustration of this single-sample Monte Carlo estimator can be found in Fig. 2.

In a complete walk, the recursive estimator begins from an arbitrary evaluation point within $\Omega \setminus \partial \Omega_D^{\epsilon}$; at each *step*, the estimator performs up to three sampling operations around the query point

- (1) Sample source contribution at point $y_{k+1} \in St$.
- (2) Sample Neumann contribution at point $z_{k+1} \in \partial St \cap \partial \Omega_N$.
- (3) Sample the next walk location $x_{k+1} \in \partial St$.

The walk continues until it reaches $\partial\Omega_{\mathrm{D}}^{\epsilon},$ where it uses the Dirichlet data g at the closest point $\bar{x}_k \in \partial \Omega_D$ to set $u(x_k) := g(\bar{x}_k)$. The first term of Eq. 2 is an unknown term that needs to be estimated recursively, similar to the scenario encountered in Monte Carlo rendering, thus we name it as recursive term. The recursive term lacks a closed form expression or shape information before computation, posing significant challenges for traditional importance sampling approaches. Therefore, in this paper, we employ guiding-based importance sampling at this term to achieve variance reduction.

3.3 von Mises-Fisher Mixture Model

We adopt the von Mises-Fisher (vMF) mixture model as the guiding distribution (see Section 4.1) due to its closed-form expression, which facilitates efficient fitting and sampling. Since PDE problems are often solved in various dimensions, we adopt the generalized form of the vMF distribution. The vMF distribution on the (d-1)sphere \mathbb{S}^{d-1} in \mathbb{R}^d (d=2,3) is defined as:

$$v(\nu \mid \mu, \kappa) = \frac{\kappa^{d/2 - 1}}{(2\pi)^{d/2} I_{d/2 - 1}(\kappa)} \exp(\kappa \mu^{\mathrm{T}} \nu), \tag{3}$$

where $v \in \mathbb{S}^{d-1}$ represents a direction, $\kappa \in [0, +\infty)$ and $\mu \in \mathbb{S}^{d-1}$ define the concentration and mean of the vMF distribution, resp., and I_k denotes the modified Bessel function of the first kind at order k. We refer to Appendix A for specific forms of vMF distribution in different dimensions. The vMF mixture model is thus a convex combination of K vMF components:

$$\mathcal{V}(\nu \mid \Theta) = \sum_{i=1}^{K} \lambda_i \cdot v(\nu \mid \mu_i, \kappa_i), \tag{4}$$

where $\Theta \in \mathbb{R}^{(2+d) \times K}$ is a set of mixture parameters, containing KvMF components, each with $\lambda_i \in [0, 1], \kappa_i \in [0, +\infty)$ and $\mu_i \in \mathbb{S}^{\bar{d}-1}$. Here, the mixture weight λ_i satisfies $\sum_i \lambda_i = 1$. The vMF mixture model is naturally defined on the sphere across various dimensions, which aligns with the directional nature of the recursive term. The vMF mixture model has already been used in the path guiding work in the rendering domain [Dong et al. 2023; Herholz et al. 2019].

4 Method

Importance Sampling the Recursive Term of the WoSt

We reparameterize the recursive term of the WoSt estimator (Eq. 2) using the unit-length vector v, yielding an estimator of the following form:

$$\langle u(x_k) \rangle = \frac{\langle u(v; x_k) \rangle}{\|\mathbb{S}^{d-1}\| \alpha(x_k) p(v \mid x_k)} - \langle N \rangle + \langle S \rangle, \tag{5}$$

where $v = \frac{x_{k+1} - x_k}{\|x_{k+1} - x_k\|} \in \mathbb{S}^{d-1}$ (d = 2, 3), and $p(v \mid x_k)$ is the directional PDF of the sampler *conditioned on* x_k . We refer to Appendix B for a detailed derivation. For $x_k \in \partial \Omega_N$ with a normal $n(x_k)$, the following condition of p is satisfied, reflecting the fact that Neumann boundaries only have one valid side in random walk:

$$p(v \mid x_k) = 0 \quad \text{when } v \cdot n(x_k) \le 0.$$
 (6)

In this formulation, the PDF of uniform directional sampling² for the recursive term adopted by original WoSt, p_u , is thus:

$$p_{\mathbf{u}}(v \mid x_k) = \begin{cases} \frac{2H(v \cdot n(x_k))}{\|\mathbb{S}^{d-1}\|}, & \text{if } x_k \in \partial \Omega_{\mathbf{N}}, \\ \frac{1}{\|\mathbb{S}^{d-1}\|}, & \text{otherwise,} \end{cases}$$
(7)

where $H(\cdot)$ is the unit step function. To reduce the variance of the recursive term, as illustrated in Fig. 3, we aim to sample from an importance distribution defined on \mathbb{S}^{d-1} , referred to as the *guiding distribution* p_{g} in our context, that approximately satisfies

$$p_{\mathbf{g}}(v \mid x_k) \propto |u(v; x_k)|. \tag{8}$$

We denote $p_t(v \mid x_k) = \frac{|u(v;x_k)|}{\int |u(v;x_k)|}$ as our *target distribution*. Section 7 discusses the absolute value symbol in Eq. 8. In the next section, we will discuss how to fit our guiding distribution to the target distribution.

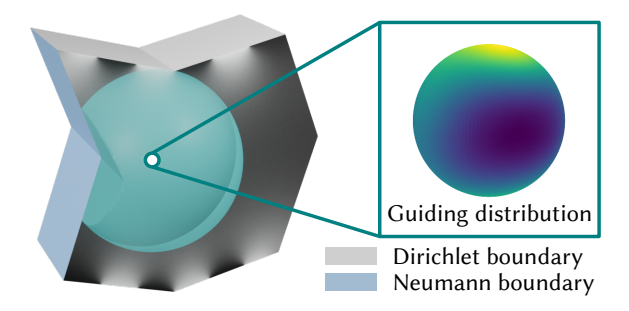


Fig. 3. Illustration of the guiding distribution at an arbitrary step. The guiding distribution is defined on \mathbb{S}^{d-1} (d=2,3), with a goal to be proportional to |u| on ∂St . The sampler uses this distribution for importance sampling.

4.2 Representing and Learning the Guiding Distribution

We adopt von Mises-Fisher (vMF) mixture model (Eq. 4) as the guiding distribution (Eq. 8) conditioned on $x \notin \partial \Omega_N$:

$$p_{g}(v \mid x) = \mathcal{V}(v \mid \Theta(x)). \tag{9}$$

where $\Theta(x)$ is the space-conditioned form of Θ in Eq. 4. To represent it, we employ a neural field $NN(x \mid \Phi)$ with trainable parameters Φ to output its predicted values $\hat{\Theta}(x)$:

$$NN(x \mid \Phi) = \hat{\Theta}(x), \tag{10}$$

where NN consists of a multi-resolution feature grid and a light-weight multi-layer perceptron (MLP). The inference and training procedure is illustrated in Fig. 4. Given a query point x, the neural field first encodes it through the multi-resolution feature grid, producing a feature vector that is then passed into the MLP. The MLP outputs a tensor of dimension $(2+d)\times K+1$, containing the unnormalized parameters of the K-component vMF mixture, including the weights λ_i' , concentrations κ_i' , and means μ_i' , as well as the selection probability c' which is used in Section 4.4. To ensure that each output component lies within a valid range, we apply a normalization mapping, as detailed in Tab. 1. The resulting vMF mixture with valid predicted parameters $\hat{\Theta}(x)$ is then used according to Jakob [2012] to sample the direction of the next walk location.

Table 1. vMF mixture parameters, their corresponding neural field outputs, and normalization mappings. $1 \le i \le K$, where K is the number of components of the vMF mixture.

Parameter NN output		Normalization mapping	
$\mu_i \in \mathbb{S}^{d-1}$ $\kappa_i \in [0, +\infty)$ $\lambda_i \in (0, 1)$	$\mu_i' \in \mathbb{R}^d$ $\kappa_i' \in \mathbb{R}$ $\lambda_i' \in \mathbb{R}$	$\mu_i = \mu'_i / \mu'_i $ $\kappa_i = \exp(\kappa'_i)$ $\lambda_i = \exp(\lambda'_i) / \sum_{j=1}^K \exp(\lambda'_j)$	
$c \in (0,1)$ (Eq. 15)	$c' \in \mathbb{R}$	$c = \operatorname{sigmoid}(c')$	

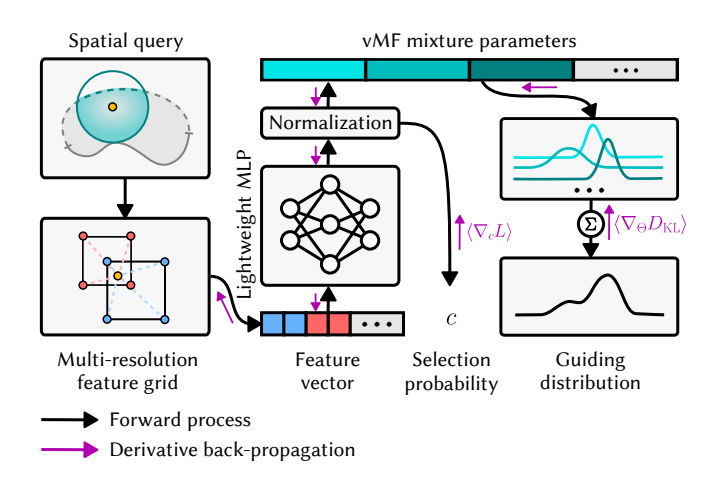


Fig. 4. Our neural field inference and training pipeline: In the forward inference step, the spatial query coordinates are encoded by a multi-resolution feature grid to produce feature vectors. These vectors are then fed into a lightweight MLP to obtain the parameters of the guiding distribution $\hat{\Theta}$ (Eq. 10) and a selection probability c (Eq. 15). During training, $\langle \nabla_{\Theta} D_{\text{KL}} \rangle$ (Eq. 13) for the guiding distribution and $\langle \nabla_{c} L \rangle$ (Eq. 17) for the selection probability are back-propagated all the way to the grid and MLP parameters

¹In this paper, we stipulate that the normal vector points toward the region where the walk is currently located. This assumption also applies to double-sided boundaries. ²The WoSt paper refers to this approach as *importance sampling the Poisson kernel*. To avoid confusion with our method, we consistently refer to the sampling approach used in the original WoSt as *uniform directional sampling* throughout this paper.

To fit the vMF mixture model V to the target distribution p_t (see Section 4.1) at x, we introduce the Kullback-Leibler (KL) divergence

$$D_{\mathrm{KL}}(p_{\mathrm{t}} \parallel \mathcal{V}; \Theta) = \int_{\mathcal{V}} p_{\mathrm{t}}(\nu) \log \frac{p_{\mathrm{t}}(\nu)}{\mathcal{V}(\nu \mid \hat{\Theta})} \mathrm{d}\nu. \tag{11}$$

The optimization objective of the neural-field parameters Φ is thus

$$\Phi^* = \underset{\Phi}{\operatorname{argmin}} \mathbb{E}_x \Big[D_{KL} \Big(p_t(x) \parallel \mathcal{V}; \Theta(x) \Big) \Big]. \tag{12}$$

We use a single-sample Monte Carlo estimator to estimate $\nabla_{\Theta} D_{\text{KL}}$:

$$\langle \nabla_{\Theta} D_{\mathrm{KL}}(p_{\mathrm{t}} \parallel \mathcal{V}; \Theta) \rangle = -\frac{p_{\mathrm{t}}(\nu) \nabla_{\Theta} \mathcal{V}(\nu \mid \hat{\Theta})}{\tilde{p}(\nu \mid \hat{\Theta}) \mathcal{V}(\nu \mid \hat{\Theta})}, \tag{13}$$

where \tilde{p} is the PDF of the sampler given by Eq. 15. We back-propagate this derivative along the purple arrows in Fig. 4, updating the parameters Φ of both the MLP and the multi-resolution feature grid using gradient-based optimization [Kingma 2014].

4.3 Sample Reflection at Neumann Boundaries

For $x \in \partial \Omega_N$, samples from the vMF mixture model span the full sphere thus do not satisfy Eq. 6. Therefore, we reflect invalid samples along the local tangent plane, resulting the following PDF:

$$p_{\mathbf{g}}(v \mid x) = \begin{cases} 0, & \text{if } v \cdot n(x) \leq 0, \\ \mathcal{V}(v^{+} \mid \Theta(x)) + \mathcal{V}(v^{-} \mid \Theta(x)), & \text{otherwise,} \end{cases}$$
(14)

where $v^+ = v$, and v^- is the reflection of v^+ off $\partial \Omega_N$ with normal n(x), i.e. $v^- = v^+ - 2(v^+ \cdot n(x)) n(x)$. We also note that a similar situation occurs in BRDF sampling of Monte Carlo rendering. However, in Dong et al. [2023]'s path guiding implementation, samples on the opposite hemisphere are directly rejected, while samples on the same hemisphere do not use the truncated vMF distribution to compute the PDF. We find that this implementation leads to significant performance degradation in PDE problems, as demonstrated by Section 6.3.1.

Multiple Importance Sampling with Learnable 4.4 Selection Probabilities

Linear elliptic equations often contain relatively smooth regions. In these regions, uniform directional sampling is sometimes the optimal approach, whereas learned vMF mixtures might yield less accurate approximation. Moreover, solely relying on the learned distribution for importance sampling is an unstable strategy, potentially introducing variance or even bias [Owen and Zhou 2000]. To address this, we introduce an learnable multiple importance sampling (MIS) method. Our approach is based on the single-sample balance heuristic [Veach and Guibas 1995b], with the following MIS PDF:

$$\tilde{p}(v \mid x) = c(x)p_{g}(v \mid x) + (1 - c(x))p_{u}(v \mid x), \tag{15}$$

where c(x) is the learnable selection probability, decoded from neural field output (Tab. 1). Following Müller et al. [2019], our method learns the selection probability at each point *x* with the following loss function:

$$L = eD_{\text{KL}}(p_t \parallel \tilde{p}) + (1 - e)D_{\text{KL}}(p_t \parallel p_g), \tag{16}$$

where e is a fixed fraction that we set to 0.2. The single-sample Monte Carlo estimator for $\nabla_c L$ for back-propagation is:

$$\langle \nabla_c L \rangle = -\frac{e p_{\rm t}(\nu) (p_{\rm g}(\nu \mid x) - p_{\rm u}(\nu \mid x))}{\tilde{p}^2(\nu \mid x)}.$$
 (17)

We find that performing our learnable MIS in combination with uniform directional sampling is sufficient to achieve excellent performance, as demonstrated in Section 6.3.2. Currently, there are no alternative importance sampling distributions for the recursive term of WoSt. We anticipate that if such distributions are developed, they could be integrated with our method using this approach. We refer to Section 7 for further discussion.

Implementation Details

Wavefront-style Monte Carlo PDE Solver

Our guiding-based method (see Section 4.2) consists of neural field inference and training, which benefits from batched input for parallelization. A common strategy in rendering for efficient batching is the wavefront-style architecture [Laine et al. 2013], where rays are generated and processed in batches. In light of this, we implement a wavefront-style Monte Carlo PDE solver on GPU.

As illustrated in Fig. 5, at each step of WoSt, our wavefront-style solver is divided into three stages:

- (1) Logic Stage: The distances to the nearest Dirichlet boundary and the Neumann silhouette are queried to compute the ball radius r (see Section 3.2). Walks are then partitioned based on whether they fall within the ϵ -shell.
- (2) Evaluation Stage: This stage resembles the Material Stage in *wavefront*-style renderers. For walks inside the ϵ -shell, contributions are evaluated on the nearest Dirichlet boundary. For walks outside the ϵ -shell, contributions from source and Neumann boundaries are evaluated.
- (3) Walk Stage: Analogous to the Ray Cast Stage in rendering, this stage samples the next walk location and updates throughput accordingly.

As each stage consists of multiple GPU kernels, we use a Structureof-Arrays (SoA) memory layout to transfer data between kernels and employ thread-safe queues to manage tasks for each kernel.

Network Design and Implementation

Neural field architecture. To effectively capture the spatial variation of the space-conditioned guiding distribution, we use a hybrid architecture combining learnable spatial embeddings and a small MLP to encode the parametric mixtures. We define L embedding grids G_l , where l = 1, 2, ..., L, to form a multi-resolution representation. Each grid spans the d-dimensional space of the problem with a spatial resolution of $D_{l}^{d}.$ A learnable embedding vector $\boldsymbol{\omega} \in \mathbb{R}^{F}$ is associated at each lattice point of G_l . To retrieve the spatial embedding for a point x, we perform bi-linear interpolation at neighboring lattice points for each resolution, and concatenate the resulting embedding vectors to form the full embedding G(x):

$$G(x \mid \Phi) = \bigoplus_{l=1}^{L} \text{bilinear}(x, V_l[x]), \quad G : \mathbb{R}^d \to \mathbb{R}^{L \times F}(d = 2, 3),$$

$$(18)$$

where $V_I[x]$ is the embedding vectors at the corners of the cell enclosing x within G_I , and \oplus is the concatenation operation. G(x) is subsequently mapped by an MLP with 3 layers, each containing 64 neurons. Trainable parameters Φ in Eq. 10 consist of the learnable spatial embeddings and MLP weights. We implement the neural field based on tiny-cuda-nn [Müller 2021], adopting DenseGrid as the encoding method of the point coordinates. We employ ReLU as the activation function of the MLP, and the output is normalized by mapping in Tab. 1, producing $\hat{\Theta}(x)$ in Eq. 10 and c(x) in Eq. 15. We refer to Appendix D for detailed configurations of the neural field.

Online training scheme. Similar to Monte Carlo rendering, walks are evaluated in batches. Each batch consists of one entire walk per evaluation point. Once all walks in a batch are completed, a training stage updates the neural field using the information gathered. The updated neural field is then used to sample the next batch. Once the walks per point (wpp) reaches a certain threshold, typically one-quarter of the total wpp, the guiding distribution converges. At this time, we terminate the training process and use the neural field exclusively for inference, further improving performance.

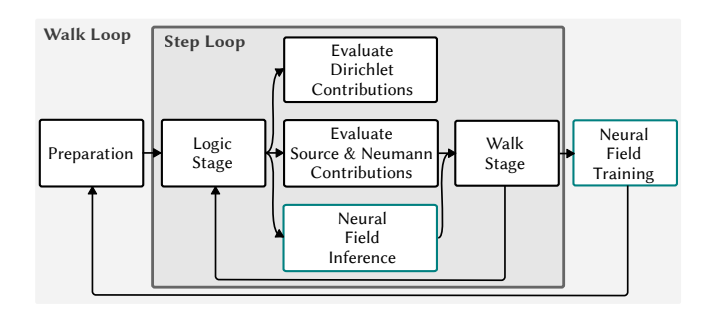


Fig. 5. Illustration of our *wavefront*-style Monte Carlo PDE solver including neural field inference and training stages.

System integration. As shown in Fig. 5, we insert the neural field inference stage before the walk stage and integrate the neural field training stage at the end of each walk loop. Our neural field and the WoSt integrator operate on separate CUDA streams, allowing the network inference and the evaluation stages to execute in parallel within the step loop. This approach maximizes the batch size during inference and training, avoiding the inefficiencies associated with single-sample inference or training.

5.3 Geometric and Source Queries

To demonstrate the practicality of our method, it is essential to implement a system with strong performance. The performance bottleneck of Monte Carlo PDE solvers typically lies in geometric queries. The authors of WoSt provide Zombie [Sawhney and Miller 2023] as the algorithm implementation and FCPW [Sawhney 2021] for geometric queries. However, Zombie is a CPU-only implementation, and although FCPW offers GPU support via Slang [He et al. 2018], integrating Slang with *tiny-cuda-nn* presents significant challenges.

To address this, we independently develop a CUDA-based geometric and source query library. For geometric queries, we reference the implementation of WoBToolbox [Sugimoto et al. 2023]

and create a comprehensive query library for WoSt using a linear BVH [Karras 2012]. While Zombie uses a dense grid for source queries in 2D, which is memory inefficient if applied in 3D, we leverage NanoVDB [Museth 2021], a widely adopted GPU-based library for sparse volumetric storage and efficient source queries in 2D and 3D.

6 Results and Discussion

We compare our method with the original WoSt under equal time and equal sample conditions using 3D geometry and 2D diffusion curve [Orzan et al. 2008] datasets. We evaluate the impact of training batch size and the number of vMF components. Additionally, ablation studies are conducted on our two key improvements: sample reflection at Neumann boundaries and learnable multiple importance sampling. We employ the relative mean squared error (relMSE) as our quantitative metric. All experiments are performed on an AMD EPYC 9754 128-Core Processor with an RTX 4090D GPU.

Since our method is the first importance sampling approach targeting the recursive term of WoSt, we find it reasonable to validate its effectiveness by comparing with the original WoSt. In Appendix C, we provide additional comparisons with selected existing variance reduction methods [Li et al. 2023; Qi et al. 2022].

We refer to Appendix E for the complete quantitative results at 1024 wpp of all experiments.

6.1 Comparison with the Original WoSt

For a fair equal-time comparison, we implement both our method and the original WoSt on the same system, and disable other sampling techniques such as control variates, adaptive sampling, and stratified sampling. Russian roulette is enabled only when the walk length exceeds 128 to prevent infinite walks in scenarios involving Neumann boundaries.

All experiments in this section are conducted with an evaluation grid of 1024×1024, running 1024 walks per point (wpp). Our approach does not involve pretraining and uses all samples to form the final result, ensuring no additional samples are required compared to the baseline.

6.1.1 3D Geometry. We adopt solving on slices [Sawhney and Crane 2020, Section 5.2] as the visualization method. For the dataset, following the experimental design of Li et al. [2023], we create six 3D problems to compare performance on Dirichlet boundaries (Fig. 6, columns 1–2), source (column 3), Neumann boundaries (columns 4–5), and problems involving both positive and negative values (column 6).

Qualitative and quantitative results are presented in Fig. 7, while Fig. 8 and Fig. 9 illustrate the relMSE as a function of wpp and as a function of time, *resp.* WoSt typically exhibits variance as salt-and-pepper noise [Miller et al. 2023], which is better visualized when zoomed in. The experimental results demonstrate that our method outperforms the original WoSt both qualitatively and quantitatively in all problems. Although our method incurs some performance costs, requiring longer runtimes at the same wpp, the results under equal time (Fig. 9) demonstrate that the variance reduction effect of our method compensates for the runtime overhead.

6.1.2 2D Diffusion Curves. We use the diffusion curves [Orzan et al. 2008] as our 2D dataset, which employs Dirichlet boundaries to fill colors in vector graphics. Neumann boundaries are added at the bounding box to prevent infinite walks. We select two representative problems: Fille and Ladybug. These problems exhibit distinct characteristics: Fille has more pronounced light-dark variations; while Ladybug features smoother variations, providing a problem more favorable for the baseline.

We report the qualitative and quantitative results in Fig. 10, present the relMSE vs. wpp plot in Fig. 11 and the relMSE vs. time plot in Fig. 12. For the Ladybug problem, initially, uniform directional sampling better matches the problem's smoothness compared to the initialization of the guiding distribution. Over time, the guiding distribution fits the higher-frequency regions, while the lowerfrequency regions shift towards using uniform directional sampling thanks to the learnable selection probabilities, allowing our method to eventually outperform the baseline.

6.2 Evaluation

6.2.1 Training Batch Size. Our method uses a fraction of batches for training, as described in Section 5.2. To assess the impact of training batch size, we vary the training batch sizes to 64, 128, 256, and 512 wpp, and compare their relMSE and runtime at 1024 wpp. The rest of the experimental setup follows Section 6.1. Fig. 13 indicates that the training steps have a significant impact on runtime, primarily because training steps are blocking (see Fig. 5). Moreover, our model converges relatively quickly, with the performance improvement from 128 wpp to 256 wpp being smaller than that from 64 wpp to 128 wpp. Therefore, using one-quarter of the total wpp as the training batch size proves to be a reasonable choice.

6.2.2 Number of vMF Components in the Mixture Model. We set the number of vMF components K, to 4, 8, and 16, and compare their relMSE and runtime at 1024 wpp with a training batch size of 256. As shown in Fig. 14, increasing the number of vMF components from 4 to 8 results in a significant improvement. However, further increasing K to 16 does not provide noticeable benefits and often leads to increased runtime.

6.3 Ablation

6.3.1 Sample Reflection at Neumann Boundaries. We qualitatively evaluate results with or without reflecting samples at Neumann boundaries in Fig. 15. The experiment shows that the method without reflection results in worse variance around the Neumann boundary than the original WoSt, while introducing reflection significantly reduces the variance.

6.3.2 Multiple Importance Sampling (MIS) with Learnable Selection Probabilities. We conduct experiments on problems in Section 6.1, with the same setup except for different sampling configurations: uniform directional sampling only (selection probabilities $c(x) \equiv 0$), fixed MIS selection probability ($c(x) \equiv 0.5$), guided sampling only $(c(x) \equiv 1)$, and our learnable MIS (c(x)) is decoded from the neural field). We report relative MSE as shown in Tab. 2. The experiments show that our learnable MIS strategy achieves the best performance.

Table 2. Quantitative results (relMSE↓) of the ablation study on MIS with learnable selection probabilities.

Problem	Uniform Only	Iniform Only Fixed $c(x) \equiv 0.5$		Ours
Bob	0.00385	0.00181	0.00136	0.00098
Bunny	0.01511	0.00690	0.00591	0.00564
Dragon	0.00353	0.00158	0.00135	0.00088
Gear	0.00153	0.00085	0.00075	0.00072
Bottle	0.00459	0.00305	0.00288	0.00274
Fille	0.00523	0.00210	0.00241	0.00208

7 Limitations and Future Work

Positivization. Our method effectively reduces shape variance; however, for real-valued integrands, we cannot eliminate sign variance with a positive-valued PDF [Owen and Zhou 2000], as shown in Fig. 16. Some recent rendering research has addressed similar issues. For instance, Belhe et al. [2024]; Zeltner et al. [2021] tackle this problem but are limited to deterministic, analytical BRDF functions. Another recent work [Fan et al. 2024] relies on the property that scattering events do not alter the sign of differential radiance in physics-based differentiable rendering to avoid branching estimators, which is inapplicable to our problem. In our problem, the target distribution at each step cannot be guaranteed to be analytic or to maintain a consistent sign in a complete walk. We note that existing sampling methods for source and boundaries of Monte Carlo PDEs do not consider positivization as well, so we believe this is beyond the scope of our work and leave it for future exploration.

Delta function and Next Event Estimation. Similar to path guiding in rendering, our method alone cannot handle delta boundaries or source. We anticipate that combining our method with Reverse Walk Splatting [Qi et al. 2022], or developing an analogy to Next Event Estimation [Immel et al. 1986; Kajiya 1986] and integrating it via multiple importance sampling, could address this issue.

More estimators. We have only discussed the importance sampling of the WoSt estimator for Poisson equations with Dirichlet and Neumann boundaries, omitting discussions on Robin boundaries [Miller et al. 2024b] and other PDEs [Sawhney et al. 2022]. However, we believe that in these forms of WoSt, the importance sampling for the recursive term is similar, and extending our method to these cases should not pose significant challenges. Additionally, there should also be a guiding-based importance sampling method for Walk on Boundary [Sugimoto et al. 2023]. For the inverse PDE estimators, drawing from differentiable path tracing, it is also expected to require different guiding strategies [Fan et al. 2024].

Importance sampling other terms. Our method performs importance sampling only on the recursive term of WoSt estimator. Although it is theoretically possible to use directional distributions to approximate the source and Neumann contributions, we do not believe this is the best strategy. On the one hand, there are already efficient sampling method for Neumann boundaries based on SNCH trees [Sawhney et al. 2023]. On the other hand, source are not merely d-1 dimensional directional distributions but rather d dimensional distributions over a star-shaped region. We believe there are better

strategies to sample source, such as using a certain form of light trees [Conty Estevez and Kulla 2018; Lin and Yuksel 2020].

Combination with other variance reduction methods. Our method reduces the variance of WoSt in the importance sampling aspect, which is not addressed by previous variance reduction research. Therefore, our method is theoretically orthogonal to existing methods. Integrating our method with existing approaches holds the potential to further reduce the variance of WoSt.

8 Conclusion

We propose a guiding-based method to importance sample the recursive term of the walk on stars (WoSt) estimator, drawing connections between Monte Carlo PDE solvers and Monte Carlo rendering. We approximate the directional distribution of the recursive term of WoSt by fitting a guiding distribution, parameterized by a neural field, to observations from previous walks. This distribution is then used to guide subsequent walks with improved sampling efficiency. A sample reflection technique is introduced to better shape the guiding distribution to align with the target distribution at Neumann boundaries. Experiments under equal time and equal sample settings show that our method effectively reduces the variance while enabling efficient GPU parallelization. The expressive guiding distribution improves sampling efficiency, particularly at positions where the solution field exhibits higher frequency. Additionally, the learnable selection probabilities adapts the balance between the uniform directional sampling and guiding to the local properties of the solution field, further reducing variance. We anticipate further advancements in variance reduction for Monte Carlo PDE solvers and believe rendering domain techniques will have broader applications across other fields.

References

- Ghada Bakbouk and Pieter Peers. 2023. Mean Value Caching for Walk on Spheres. In Eurographics Symposium on Rendering, Tobias Ritschel and Andrea Weidlich (Eds.). The Eurographics Association. https://doi.org/10.2312/sr.20231120
- Mégane Bati, Stéphane Blanco, Christophe Coustet, Vincent Eymet, Vincent Forest, Richard Fournier, Jacques Gautrais, Nicolas Mellado, Mathias Paulin, and Benjamin Piaud. 2023. Coupling Conduction, Convection and Radiative Transfer in a Single Path-Space: Application to Infrared Rendering. ACM Trans. Graph. 42, 4, Article 79 (July 2023), 20 pages. https://doi.org/10.1145/3592121
- Yash Belhe, Bing Xu, Sai Praveen Bangaru, Ravi Ramamoorthi, and Tzu-Mao Li. 2024. Importance Sampling BRDF Derivatives. ACM Trans. Graph. 43, 3, Article 25 (April 2024), 21 pages. https://doi.org/10.1145/3648611
- Donald Best and Nicholas Fisher. 1979. Efficient Simulation of the von Mises Distribution. *Journal of the Royal Statistical Society. Series C. Applied Statistics* 28 (01 1979). https://doi.org/10.2307/2346732
- Alejandro Conty Estevez and Christopher Kulla. 2018. Importance Sampling of Many Lights with Adaptive Tree Splitting. *Proc. ACM Comput. Graph. Interact. Tech.* 1, 2, Article 25 (Aug. 2018), 17 pages. https://doi.org/10.1145/3233305
- Fernando de Goes and Mathieu Desbrun. 2024. Stochastic Computation of Barycentric Coordinates. ACM Trans. Graph. 43, 4, Article 42 (July 2024), 13 pages. https://doi.org/10.1145/3658131
- Auguste De Lambilly, Gabriel Benedetti, Nour Rizk, Chen Hanqi, Siyuan Huang, Junnan Qiu, David Louapre, Raphael Granier De Cassagnac, and Damien Rohmer. 2023. Heat Simulation on Meshless Crafted-Made Shapes. In Proceedings of the 16th ACM SIGGRAPH Conference on Motion, Interaction and Games (Rennes, France) (MIG '23). Association for Computing Machinery, New York, NY, USA, Article 9, 7 pages. https://doi.org/10.1145/3623264.3624457
- Honghao Dong, Rui Su, Guoping Wang, and Sheng Li. 2024. Efficient Neural Path Guiding with 4D Modeling. In SIGGRAPH Asia 2024 Conference Papers (SA '24). Association for Computing Machinery, New York, NY, USA, Article 21, 11 pages. https://doi.org/10.1145/3680528.3687687
- Honghao Dong, Guoping Wang, and Sheng Li. 2023. Neural Parametric Mixtures for Path Guiding. In ACM SIGGRAPH 2023 Conference Proceedings (Los Angeles, CA,

- USA) (SIGGRAPH '23). Association for Computing Machinery, New York, NY, USA, Article 29, 10 pages. https://doi.org/10.1145/3588432.3591533
- S. Ermakov and A. Sipin. 2009. The "walk in hemispheres" process and its applications to solving boundary value problems. Vestnik St. Petersburg University: Mathematics 42 (09 2009), 155–163. https://doi.org/10.3103/S1063454109030029
- Zhimin Fan, Pengpei Hong, Jie Guo, Changqing Zou, Yanwen Guo, and Ling-Qi Yan. 2023. Manifold Path Guiding for Importance Sampling Specular Chains. *ACM Trans. Graph.* 42, 6, Article 257 (Dec. 2023), 14 pages. https://doi.org/10.1145/3618360
- Zhimin Fan, Pengcheng Shi, Mufan Guo, Ruoyu Fu, Yanwen Guo, and Jie Guo. 2024.
 Conditional Mixture Path Guiding for Differentiable Rendering. ACM Trans. Graph.
 43, 4, Article 48 (July 2024), 11 pages. https://doi.org/10.1145/3658133
- Yong He, Kayvon Fatahalian, and Tim Foley. 2018. Slang: language mechanisms for extensible real-time shading systems. ACM Trans. Graph. 37, 4, Article 141 (July 2018), 13 pages. https://doi.org/10.1145/3197517.3201380
- Sebastian Herholz, Yangyang Zhao, Oskar Elek, Derek Nowrouzezahrai, Hendrik P. A. Lensch, and Jaroslav Křivánek. 2019. Volume Path Guiding Based on Zero-Variance Random Walk Theory. ACM Trans. Graph. 38, 3, Article 25 (June 2019), 19 pages. https://doi.org/10.1145/3230635
- Heinrich Hey and Werner Purgathofer. 2002. Importance sampling with hemispherical particle footprints. In *Proceedings of the 18th Spring Conference on Computer Graphics* (Budmerice, Slovakia) (SCCG '02). Association for Computing Machinery, New York, NY, USA, 107–114. https://doi.org/10.1145/584458.584476
- Jiawei Huang, Akito Iizuka, Hajime Tanaka, Taku Komura, and Yoshifumi Kitamura. 2024. Online Neural Path Guiding with Normalized Anisotropic Spherical Gaussians. ACM Trans. Graph. 43, 3, Article 26 (April 2024), 18 pages. https://doi.org/10.1145/ 3649310
- Yuchi Huo, Rui Wang, Ruzahng Zheng, Hualin Xu, Hujun Bao, and Sung-Eui Yoon. 2020. Adaptive Incident Radiance Field Sampling and Reconstruction Using Deep Reinforcement Learning. ACM Trans. Graph. 39, 1, Article 6 (Jan. 2020), 17 pages. https://doi.org/10.1145/3368313
- David S. Immel, Michael F. Cohen, and Donald P. Greenberg. 1986. A radiosity method for non-diffuse environments. In Proceedings of the 13th Annual Conference on Computer Graphics and Interactive Techniques (SIGGRAPH '86). Association for Computing Machinery, New York, NY, USA, 133–142. https://doi.org/10.1145/15922. 15901
- Pranav Jain, Ziyin Qu, Peter Yichen Chen, and Oded Stein. 2024. Neural Monte Carlo Fluid Simulation. In ACM SIGGRAPH 2024 Conference Papers (Denver, CO, USA) (SIGGRAPH '24). Association for Computing Machinery, New York, NY, USA, Article 9, 11 pages. https://doi.org/10.1145/3641519.3657438
- Wenzel Jakob. 2012. Numerically stable sampling of the von Mises-Fisher distribution on S^2 (and other tricks). *Interactive Geometry Lab, ETH Zürich, Tech. Rep* (2012), 6. Henrik Wann Jensen. 1995. Importance Driven Path Tracing using the Photon Map. In
- Rendering Techniques. https://api.semanticscholar.org/Corpusib:9344202
- James T. Kajiya. 1986. The rendering equation. In Proceedings of the 13th Annual Conference on Computer Graphics and Interactive Techniques (SIGGRAPH '86). Association for Computing Machinery, New York, NY, USA, 143–150. https://doi.org/10.1145/15922.15902
- Tero Karras. 2012. Maximizing parallelism in the construction of BVHs, octrees, and k-d trees. In Proceedings of the Fourth ACM SIGGRAPH/Eurographics Conference on High-Performance Graphics (Paris, France) (EGGH-HPG'12). Eurographics Association, Goslar, DEU, 33–37.
- Diederik P Kingma. 2014. Adam: A method for stochastic optimization. arXiv preprint arXiv:1412.6980 (2014).
- Samuli Laine, Tero Karras, and Timo Aila. 2013. Megakernels considered harmful: wavefront path tracing on GPUs. In *Proceedings of the 5th High-Performance Graphics Conference* (Anaheim, California) (*HPG '13*). Association for Computing Machinery, New York, NY, USA, 137–143. https://doi.org/10.1145/2492045.2492060
- He Li, Beibei Wang, Changehe Tu, Kun Xu, Nicolas Holzschuch, and Ling-Qi Yan. 2022. Unbiased Caustics Rendering Guided by Representative Specular Paths. In Proceedings of SIGGRAPH Asia 2022.
- Zilu Li, Guandao Yang, Xi Deng, Christopher De Sa, Bharath Hariharan, and Steve Marschner. 2023. Neural Caches for Monte Carlo Partial Differential Equation Solvers. In SIGGRAPH Asia 2023 Conference Papers (Sydney, NSW, Australia) (SA '23). Association for Computing Machinery, New York, NY, USA, Article 34, 10 pages. https://doi.org/10.1145/3610548.3618141
- Daqi Lin and Cem Yuksel. 2020. Real-Time Stochastic Lightcuts. Proc. ACM Comput. Graph. Interact. Tech. (Proceedings of I3D 2020) 3, 1 (2020), 18 pages. https://doi.org/ 10.1145/3384543
- Bailey Miller, Rohan Sawhney, Keenan Crane, and Ioannis Gkioulekas. 2023. Boundary Value Caching for Walk on Spheres. ACM Trans. Graph. 42, 4 (2023).
- Bailey Miller, Rohan Sawhney, Keenan Crane, and Ioannis Gkioulekas. 2024a. Differential Walk on Spheres. ACM Trans. Graph. 43, 6 (2024).
- Bailey Miller, Rohan Sawhney, Keenan Crane, and Ioannis Gkioulekas. 2024b. Walkin' Robin: Walk on Stars with Robin Boundary Conditions. ACM Trans. Graph. 43, 4 (2024).

- Rafael I. Cabral Muchacho and Florian T. Pokorny. 2024. Walk on Spheres for PDE-based Path Planning. arXiv:2406.01713 [cs.RO] https://arxiv.org/abs/2406.01713
- Mervin E. Muller. 1956. Some Continuous Monte Carlo Methods for the Dirichlet Problem. The Annals of Mathematical Statistics 27, 3 (1956), 569 - 589. https://doi.org/10.1001/ //doi.org/10.1214/aoms/1177728169
- Thomas Müller. 2021. tiny-cuda-nn. https://github.com/NVlabs/tiny-cuda-nn
- Thomas Müller, Markus Gross, and Jan Novák. 2017. Practical Path Guiding for Efficient Light-Transport Simulation. Computer Graphics Forum (Proceedings of EGSR) 36, 4 (June 2017), 91-100. https://doi.org/10.1111/cgf.13227
- Thomas Müller, Brian McWilliams, Fabrice Rousselle, Markus Gross, and Jan Novák. 2019. Neural Importance Sampling. ACM Trans. Graph. 38, 5, Article 145 (Oct. 2019), 19 pages. https://doi.org/10.1145/3341156
- Thomas Müller, Fabrice Rousselle, Jan Novák, and Alexander Keller. 2021. Real-time neural radiance caching for path tracing. ACM Trans. Graph. 40, 4, Article 36 (July 2021), 16 pages. https://doi.org/10.1145/3450626.3459812
- Ken Museth. 2021. NanoVDB: A GPU-Friendly and Portable VDB Data Structure For Real-Time Rendering And Simulation. In ACM SIGGRAPH 2021 Talks (Virtual Event, USA) (SIGGRAPH '21). Association for Computing Machinery, New York, NY, USA, Article 1, 2 pages. https://doi.org/10.1145/3450623.3464653
- Mohammad Sina Nabizadeh, Ravi Ramamoorthi, and Albert Chern. 2021. Kelvin transformations for simulations on infinite domains. ACM Transactions on Graphics (TOG) 40, 4 (2021), 97:1-97:15.
- Hong Chul Nam, Julius Berner, and Anima Anandkumar. 2024. Solving Poisson Equations Using Neural Walk-on-Spheres. In Forty-first International Conference on Machine Learning.
- Alexandrina Orzan, Adrien Bousseau, Holger Winnemöller, Pascal Barla, Joëlle Thollot, and David Salesin. 2008. Diffusion curves: a vector representation for smooth-shaded images, In ACM SIGGRAPH 2008 Papers (Los Angeles, California) (SIGGRAPH '08). Association for Computing Machinery, New York, NY, USA, Article 92, 8 pages. https://doi.org/10.1145/1399504.1360691
- Art Owen and Yi Zhou. 2000. Safe and Effective Importance Sampling. J. Amer. Statist. Assoc. 95, 449 (2000), 135-143. http://www.jstor.org/stable/2669533
- Adam Paszke, Sam Gross, Francisco Massa, Adam Lerer, James Bradbury, Gregory Chanan, Trevor Killeen, Zeming Lin, Natalia Gimelshein, Luca Antiga, Alban Desmaison, Andreas Köpf, Edward Yang, Zach DeVito, Martin Raison, Alykhan Tejani, Sasank Chilamkurthy, Benoit Steiner, Lu Fang, Junjie Bai, and Soumith Chintala. 2019. PyTorch: an imperative style, high-performance deep learning library. Curran Associates Inc., Red Hook, NY, USA.
- Yang Qi, Dario Seyb, Benedikt Bitterli, and Wojciech Jarosz. 2022. A bidirectional formulation for Walk on Spheres. Computer Graphics Forum (Proceedings of EGSR) 41, 4 (July 2022). https://doi.org/10/jgzr
- Alexander Rath, Pascal Grittmann, Sebastian Herholz, Petr Vévoda, Philipp Slusallek, and Jaroslav Křivánek. 2020. Variance-aware path guiding. ACM Trans. Graph. 39, 4, Article 151 (Aug. 2020), 12 pages. https://doi.org/10.1145/3386569.3392441
- Florian Reibold, Johannes Hanika, Alisa Jung, and Carsten Dachsbacher. 2018. Selective guided sampling with complete light transport paths. ACM Trans. Graph. 37, 6, Article 223 (Dec. 2018), 14 pages. https://doi.org/10.1145/3272127.3275030
- Damien Rioux-Lavoie, Ryusuke Sugimoto, Tümay Özdemir, Naoharu H. Shimada, Christopher Batty, Derek Nowrouzezahrai, and Toshiya Hachisuka. 2022. A Monte Carlo Method for Fluid Simulation. ACM Transactions on Graphics 41, 6 (Dec. 2022). https://doi.org/10.1145/3550454.3555450
- Rohan Sawhney. 2021. FCPW: Fastest Closest Points in the West.
- Rohan Sawhney and Keenan Crane. 2020. Monte Carlo Geometry Processing: A Grid-Free Approach to PDE-Based Methods on Volumetric Domains. ACM Trans. Graph.
- Rohan Sawhney and Bailey Miller. 2023. Zombie: A Grid-Free Monte Carlo Solver for
- Rohan Sawhney, Bailey Miller, Ioannis Gkioulekas, and Keenan Crane. 2023. Walk on Stars: A Grid-Free Monte Carlo Method for PDEs with Neumann Boundary Conditions. ACM Trans. Graph. 42, 4 (2023).
- Rohan Sawhney, Dario Seyb, Wojciech Jarosz, and Keenan Crane. 2022. Grid-Free Monte Carlo for PDEs with Spatially Varying Coefficients. ACM Trans. Graph. XX,
- Nikolai A. Simonov. 2008. Walk-on-Spheres Algorithm for Solving Boundary-Value Problems with Continuity Flux Conditions. https://api.semanticscholar.org/
- Ryusuke Sugimoto, Christopher Batty, and Toshiya Hachisuka. 2024a. Velocity-Based Monte Carlo Fluids. In ACM SIGGRAPH 2024 Conference Papers (Denver, CO, USA) (SIGGRAPH '24). Association for Computing Machinery, New York, NY, USA, Article 8, 11 pages. https://doi.org/10.1145/3641519.3657405
- Ryusuke Sugimoto, Terry Chen, Yiti Jiang, Christopher Batty, and Toshiya Hachisuka. 2023. A Practical Walk-on-Boundary Method for Boundary Value Problems. ACM Trans. Graph. 42, 4, Article 81 (jul 2023), 16 pages. https://doi.org/10.1145/3592109
- Ryusuke Sugimoto, Nathan King, Toshiya Hachisuka, and Christopher Batty. 2024b. Projected Walk on Spheres: A Monte Carlo Closest Point Method for Surface PDEs. In ACM SIGGRAPH Asia 2024 Conference Papers (Tokyo, Japan) (SIGGRAPH Asia

- '24). Association for Computing Machinery, New York, NY, USA, 10 pages. https:// //doi.org/10.1145/3680528.3687599
- Eric Veach. 1998. Robust Monte Carlo methods for light transport simulation. Stanford University.
- Eric Veach and Leonidas Guibas. 1995a. Bidirectional Estimators for Light Transport. In Photorealistic Rendering Techniques, Georgios Sakas, Stefan Müller, and Peter Shirley (Eds.). Springer Berlin Heidelberg, Berlin, Heidelberg, 145-167.
- Eric Veach and Leonidas J. Guibas. 1995b. Optimally combining sampling techniques for Monte Carlo rendering. In Proceedings of the 22nd Annual Conference on Computer Graphics and Interactive Techniques (SIGGRAPH '95). Association for Computing Machinery, New York, NY, USA, 419-428. https://doi.org/10.1145/218380.218498
- Jiří Vorba, Ondřej Karlík, Martin Šik, Tobias Ritschel, and Jaroslav Křivánek. 2014. On-line learning of parametric mixture models for light transport simulation. ACM Trans. Graph. 33, 4, Article 101 (July 2014), 11 pages. https://doi.org/10.1145/2601097. 2601203
- Ekrem Fatih Yilmazer, Delio Vicini, and Wenzel Jakob. 2024. Solving Inverse PDE Problems using Monte Carlo Estimators. Transactions on Graphics (Proceedings of SIGGRAPH Asia) 43 (Dec. 2024). https://doi.org/10.1145/3687990
- Z. Yu, L. Wu, Z. Zhou, and S. Zhao. 2024. A Differential Monte Carlo Solver For the Poisson Equation. In ACM SIGGRAPH 2024 Conference Proceedings.
- Tizian Zeltner, Sébastien Speierer, Iliyan Georgiev, and Wenzel Jakob. 2021. Monte Carlo Estimators for Differential Light Transport. Transactions on Graphics (Proceedings of SIGGRAPH) 40, 4 (Aug. 2021). https://doi.org/10.1145/3450626.3459807
- Shilin Zhu, Zexiang Xu, Tiancheng Sun, Alexandr Kuznetsov, Mark Meyer, Henrik Wann Jensen, Hao Su, and Ravi Ramamoorthi. 2021. Hierarchical neural reconstruction for path guiding using hybrid path and photon samples. ACM Trans. Graph. 40, 4, Article 35 (July 2021), 16 pages. https://doi.org/10.1145/3450626.3459810

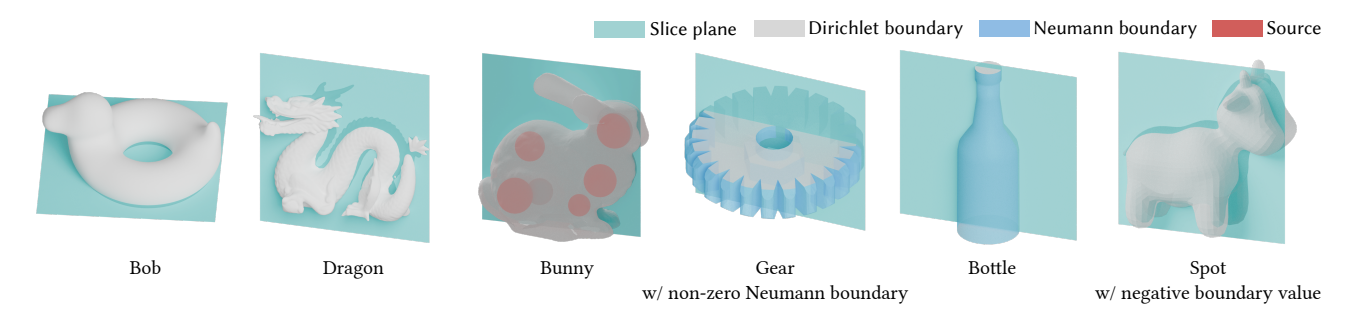


Fig. 6. Dataset for our 3D experiments. We adopt solving on slices [Sawhney and Crane 2020, Section 5.2] as the visualization method.

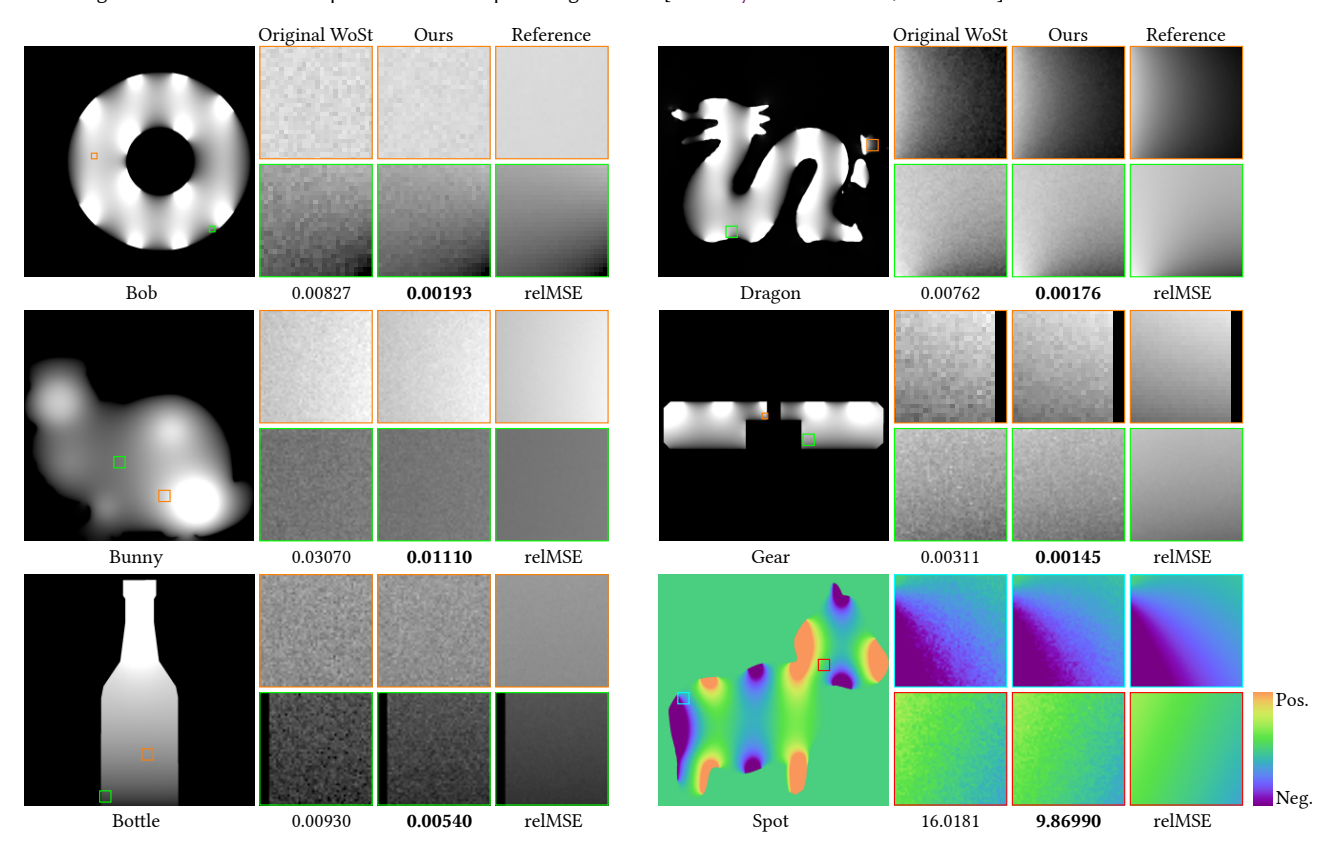


Fig. 7. Qualitative results of our 3D experiments at 512 wpp. We follow Sawhney and Crane [2020, Fig. 6], using grayscale images to visualize the solution. Since WoSt typically exhibits variance as uniform salt-and-pepper noise [Sawhney et al. 2023, Section 4], we zoom in on representative regions for visualization. We report relMSE at 512 wpp for each problem below the corresponding images.

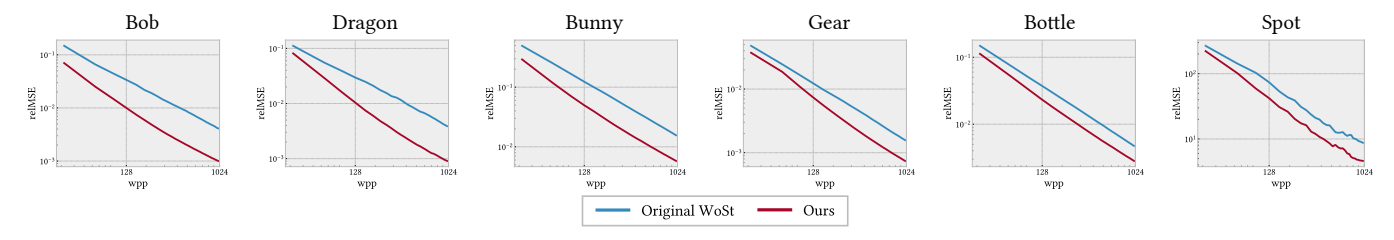


Fig. 8. relMSE plotted as a function of wpp of our 3D experiments. Under the condition of equal wpp, our method comprehensively surpasses the original WoSt in 3D problems. In the best scenario, it achieves more than a 4× reduction in variance, while in problems with relatively uniform solution distributions, it still delivers approximately a 2× improvement.

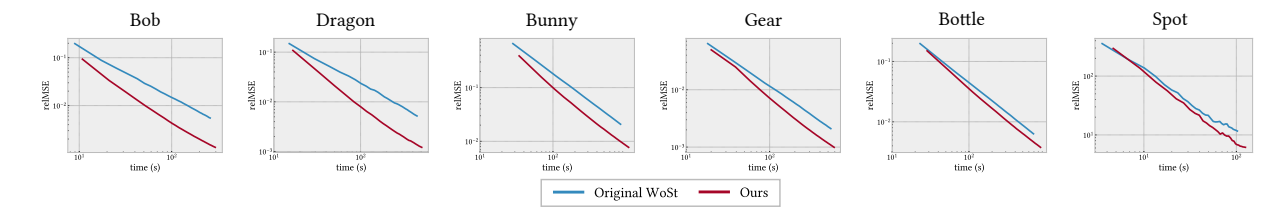


Fig. 9. relMSE plotted as a function of time of our 3D experiments. Despite the performance overhead, our method still maintains an advantage in equal-time comparisons across all 3D problems.

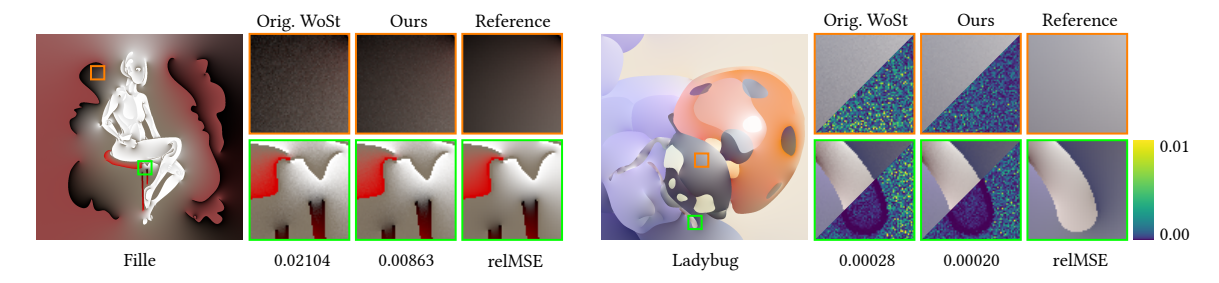


Fig. 10. The qualitative and quantitative results of the 2D diffusion curve experiments at 256 wpp. We present the rendering results of two examples at this wpp and report their relMSE. Due to the rapid convergence of Ladybug, the noise of both methods is nearly imperceptible. To facilitate comparison, we also present false-color maps of the per-pixel relative squared error.

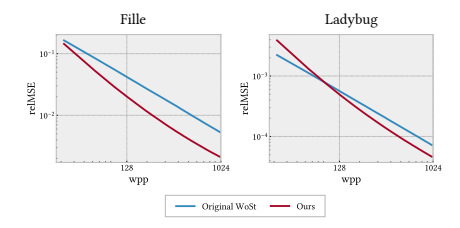


Fig. 11. relMSE plotted as a function of wpp of our diffusion curve experiments. Most regions in the Ladybug problem are well-suited for uniform directional sampling, however, our method achieves better results after a short amount of wpp.

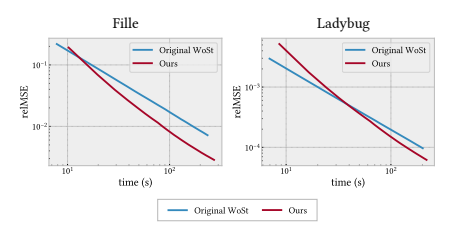


Fig. 12. relMSE plotted as a function of time of our diffusion curve experi-

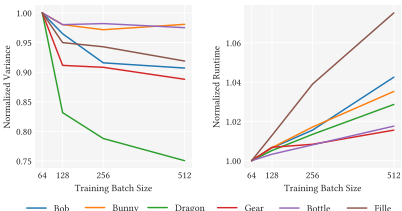


Fig. 13. The evaluation experiment results for training batch size. We normalize the results by the data with the batch size of 64.



Fig. 14. The evaluation experiment results for the number of vMFs. We normalize the results by the data with the number of 4.



Fig. 15. Ablation experiment results for the sample reflection at the Neumann boundaries. We show qualitative results of the patch near a Neumann boundary, and report their relMSE.

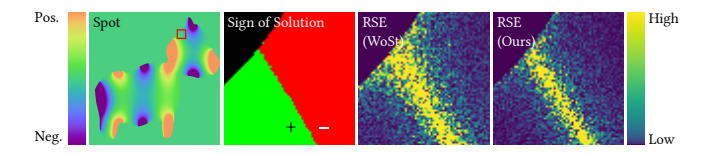


Fig. 16. Limitation: Our method effectively reduces shape variance, but like the baseline original WoSt, it cannot reduce sign variance.

A von Mises-Fisher (vMF) Distribution

Below, we present the 2D and 3D formulations of the vMF distribution: $\,$

$$v^{\text{2D}}(\nu \mid \mu, \kappa) = \frac{\exp(\kappa \mu^{\text{T}} \nu)}{2\pi I_0(\kappa)},$$

$$v^{\mathrm{3D}}(\nu \mid \mu, \kappa) = \frac{\kappa}{4\pi \sinh \kappa} \exp(\kappa \mu^{\mathrm{T}} \nu).$$

The 2D vMF distribution does not have a closed-form expression. Best and Fisher [1979] provide an effective method for its computation.

B Derivation of the Reparametrization of the Walk on Stars Estimator

The Boundary Integral Formulation [Sawhney et al. 2023] for the Poisson equation is given as:

$$\alpha(x)u(x) = \int_{\partial St(x,r)} P^B(x,z)u(z)dz - \int_{\partial St_N(x,r)} G^B(x,z)h(z) dz + \int_{St(x,r)} G^B(x,y)f(y) dy.$$

The first term, which is:

$$u_1(x) = \frac{1}{\alpha(x)} \int_{\partial St(x,r)} P^B(x,z) u(z) dz,$$

corresponds to the recursive Monte Carlo integration in the WoSt estimator. Consider the 3D case. Substituting

$$P^{B,3D}(x,z) = \frac{n_z \cdot (z-x)}{4\pi ||z-x||^3}$$

into $u_1(x)$, we obtain:

$$u_1(x) = \frac{1}{\alpha(x)} \int_{\partial St(x,r)} \frac{n_z \cdot (z-x)}{4\pi ||z-x||^3} u(z) dz.$$

We perform a change of variables by letting $\frac{z-x}{\|z-x\|} = v$ and setting $\|z-x\| = r$, which gives:

$$u_1(x) = \frac{1}{\|\mathbb{S}^2\|\alpha(x)} \int_{\partial St(x,r)} u(v;x) \frac{(n_z \cdot v) dz}{r^2}$$
$$= \frac{1}{\|\mathbb{S}^2\|\alpha(x)} \int_{\mathbb{S}^2} u(v;x) dv.$$

Its corresponding single-sample Monte Carlo estimator is:

$$\langle u_1(x) \rangle = \frac{\langle u(v;x) \rangle}{\|\mathbb{S}^2\| \alpha(x) p^{\mathbb{S}^2}(v \mid x)}.$$

The 2D case follows similarly. We note that a similar derivation [Veach 1998] also exists in the Monte Carlo rendering domain.

C Comparison with Existing Variance Reduction Methods

As described in Section 6, we have chosen to compare our method only with the original WoSt in the main text of this paper. This decision is based on several factors: our approach is not a replacement or refinement of existing methods, but orthogonal to them; moreover, our method and existing approaches are implemented on different systems, making a fair comparison challenging. These challenges have also been noted by Bakbouk and Peers [2023, Section 10]. Nevertheless, to demonstrate the distinguishing features of our method, in this section, we conduct a few comparison with selected existing methods using metrics that are as comparable as possible.

C.1 Neural Caches

Neural Caches [Li et al. 2023] is another variance reduction method for WoSt that leverages a neural field. However, unlike our approach, which uses a neural field to encode a space-conditioned guiding distribution, Neural Caches directly employs a neural field to cache the solution value field in space. Unlike our online training approach, where training and inference occur progressively and simultaneously, Neural Caches explicitly separates the solving process into distinct training and inference stages. This distinction makes cross-system comparisons challenging. Therefore, we decide to pretrain a Neural Caches checkpoint and then use its inference stage to perform a comparison with our method under equal wpp condition.

Since the authors of Neural Caches have not released their code, we reproduce their work using PyTorch [Paszke et al. 2019]. We train and evaluate their approach on a 2D Laplace problem following the exact methodology described in their paper. Consistent with the design of their experiments in the original paper, we set the hyperparameter m = 1 or m = 5, meaning that performing 1 or 5 steps, *resp.*, before querying the neural field cache. The experimental results are presented in Fig. 17, where we illustrate the problem setting, the convergence plots of different methods, and a qualitative and quantitative comparison of relMSE at 256 wpp and 2048 wpp.

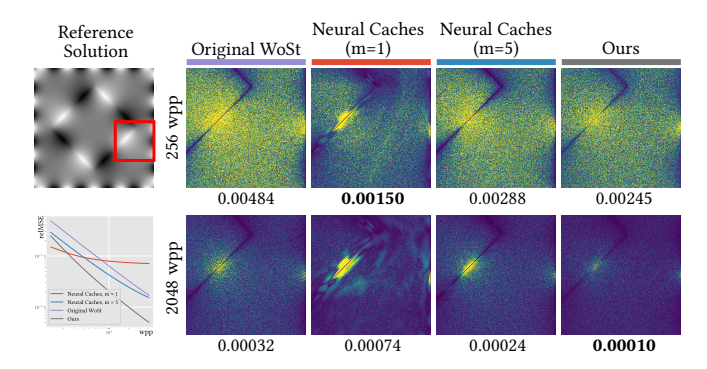


Fig. 17. Comparison with Neural Caches [Li et al. 2023] in a 2D problem.

The convergence plot aligns with the results reported by Li et al. [2023, Section 7.3 and 7.4]. The experiment demonstrates that pre-trained Neural Caches can reduce variance at low sample counts. However, due to the expressive limitations of PINNs, the solution

field cached by Neural Caches exhibits bias, which becomes increasingly evident at higher sample counts, eventually allowing the original WoSt to outperform it. Our method does not introduce additional bias, and by significantly improving the convergence rate of WoSt, greatly narrows the advantage range of Neural Caches. As shown in this experiment, our approach surpasses Neural Caches (m = 1) at approximately 100–200 wpp and is always better than Neural Caches (m = 5).

C.2 Reverse Walk Splatting

Reverse Walk Splatting (RWS) [Qi et al. 2022] adopts a strategy opposite to those of the original WoSt and ours, performing random walks from boundaries and source rather than from the evaluation points. This approach demonstrates strong performance in 2D scenarios, as the sampling space of boundaries and source is often smaller than or comparable to that of the evaluation grid, and it is easy for reverse walks to fall on the evaluation grid. However, in 3D scenarios, particularly when solving on slices [Sawhney and Crane 2020, Section 5.2], the sampling space of boundaries and source may exceed that of the evaluation grid. Besides, in 3D, the contributions from reverse walks are less likely to fall on the evaluation grid, leading to overhead and performance degradation. To illustrate this, we design a simple experiment, as shown on the far-left side of Fig. 18.

RWS does not have the concept of wpp, i.e. the number of samples per evaluation point. Therefore, we manage to achieve fairness by adjusting the number of sampling points originating from boundaries and source. In our experiment, we apply the following method to match the sample count: for RWS, we set the number of sample points on the Dirichlet boundaries to $256 \times 256 \times 1024$. Since there are no Neumann boundaries or source in this problem, we set the number of their sample points to 0. For the original WoSt and our method, we perform 1024 samples on a 256×256 evaluation grid. The experimental results are shown in Fig. 18.

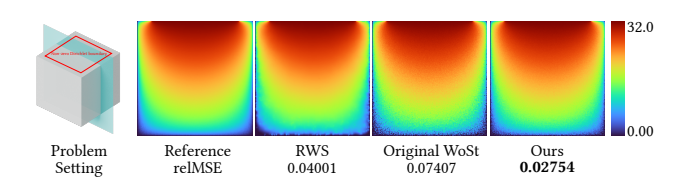


Fig. 18. Comparison with Reverse Walk Splatting (RWS) [Qi et al. 2022] in a 3D problem. Although RWS produces smooth results, correlation artifacts are observed. In this experiment, the quantitative metric for RWS outperforms the original WoSt, but is weaker than ours.

The experimental results of this problem align with our previous analysis, demonstrating that in 3D scenarios involving solving on slices where the evaluation grid has a relatively small sampling space, our method outperforms RWS both qualitatively and quantitatively under the same number of samples. Additionally, our approach avoids noticeable correlation artifacts. Our method retains the advantages of the original WoSt by not introducing unnecessary sampling.

Detailed Configurations of Our Neural Field

In this section, we present the detailed configuration of our neural field. Tab. 3 lists the configuration parameters for the multiresolution feature grid, Tab. 4 presents the parameters for the multilayer perceptron (MLP), and Tab. 5 specifies the optimizer settings. We acknowledge that an optimal set of parameters may vary depending on the dimensionality and nature of the problem. However, to demonstrate the general applicability of our approach, we have employed the same set of parameters across all experiments.

Table 3. Encoding Parameters. The Per Level Scale is utilized to generate the sequence of D_I^d . For instance, under this configuration, $D_8^d = \lfloor D_1^d \times D_1^d \rfloor$ $1.405^{(8-1)} \rfloor = 86.$

Parameter	Value
Encoding	
Base Resolution D_1^d	8
Interpolation	Linear
Features per Level F	4
Number of Levels L	8
Type	DenseGrid
Per Level Scale	1.405

Table 4. MLP Parameters. FullyFusedMLP is a high-performance MLP implementation provided by tiny-cuda-nn [Müller 2021]. The Activation here does not apply to the last layer, as the last layer employs our custom-defined normalization mappings.

Parameter	Value
Activation	ReLU
Activation Hidden Layers	3
Neurons	64
Type	FullyFusedMLP

Table 5. Optimizer Parameters.

Parameter	Value			
Optimizer				
Decay	0.95			
Type	Ema			
Nested Optimizer	r (Adam)			
AdaBound	False			
Beta1	0.9			
Beta2	0.99			
Epsilon	1.0e-15			
L2 Regularization	1.0e-6			
Learning Rate	0.008			
Туре	Adam			

E Raw Quantitative Data of Experiments

In this section, we present the complete quantitative experimental results (at 1024 wpp) corresponding to the experiments in the main text. We report both the relative MSE and the runtime. Following the order of the original paper, the results are shown in Tab. 6, Tab. 7, Tab. 8, and Tab. 9.

Table 6. Raw quantitative data of the 3D geometry experiments at 1024 wpp.

	relative N	ИSE	Runtime (s)		
Problem	Original WoSt Ours		Original WoSt	Ours	
Bob	0.003992	0.000981	268.93	305.24	
Bunny	0.015115	0.005643	868.52	1119.8	
Dragon	0.003789	0.000878	461.55	523.27	
Gear	0.001528	0.000720	555.55	609.04	
Bottle	0.004593	0.002743	712.34	879.42	
Spot	8.275137	4.157117	105.67	129.14	

Table 7. Raw quantitative data of the 2D diffusion curve experiments at 1024 wpp.

	relative	MSE	Runtime ((s)
Problem	Original WoSt Ours		Original WoSt	Ours
Fille Ladybug	$\begin{array}{ c c c c c c c c c c c c c c c c c c c$	$0.002084 \\ 4.506 \times 10^{-5}$	242.86 207.33	280.68 225.11

Table 8. Raw quantitative data of the training batch size evaluation experiments at 1024 wpp.

	relative MSE			Runtime (s)				
Problem	64	128	256	512	64	128	256	512
Bob	0.001060	0.001023	0.000971	0.000961	293.65	295.56	298.22	306.14
Bunny	0.005725	0.005612	0.005563	0.005615	1087.3	1094.5	1105.9	1125.6
Dragon	0.001185	0.000985	0.000934	0.000889	510.56	513.19	517.41	525.17
Gear	0.000790	0.000720	0.000717	0.000702	597.70	601.78	602.69	607.00
Bottle	0.002817	0.002761	0.002767	0.002747	867.83	870.67	874.82	883.10
Fille	0.002243	0.002130	0.002114	0.002060	264.80	268.20	275.12	284.71

Table 9. Raw quantitative data of the number of vMF components evaluation experiments at 1024 wpp.

	ı	elative MSI	Runtime (s)			
Problem	4 8 16		16	4	8	16
Bob	0.001107	0.000957	0.000949	294.73	298.14	302.18
Bunny	0.005731	0.005559	0.005576	1103.5	1111.4	1115.5
Dragon	0.001185	0.000887	0.000894	514.68	517.39	523.06
Gear	0.000730	0.000703	0.000703	604.77	602.70	599.60
Bottle	0.002824	0.002732	0.002691	871.54	876.53	874.91
Fille	0.002096	0.002090	0.002084	298.60	269.08	274.85